



# Electrochemical performances and mechanisms of $\text{MnSn}_2$ as anode material for Li-ion batteries



Abdelfattah Mahmoud<sup>a,c</sup>, Mohamad Chamas<sup>a</sup>, Jean-Claude Jumas<sup>a</sup>, Bertrand Philippe<sup>b</sup>, Rémi Dedryvère<sup>b</sup>, Danielle Gonbeau<sup>b</sup>, Ismael Saadoun<sup>c</sup>, Pierre-Emmanuel Lippens<sup>a,\*</sup>

<sup>a</sup> Institut Charles Gerhardt, UMR 5253 CNRS, Université Montpellier 2, Place Eugène Bataillon, 34095 Montpellier cedex 5, France

<sup>b</sup> IPREM-ECP, UMR 5254 CNRS, Université de Pau, Hélioparc, 2 av. Pierre Angot, 64053 Pau cedex 9, France

<sup>c</sup> Laboratoire de Chimie des Matériaux et de l'Environnement, Université Cadi Ayyad, Avenue A. Khattabi, BP 549 Marrakech, Morocco

## HIGHLIGHTS

- $\text{MnSn}_2$  as anode material for Li-ion batteries.
- New synthesis method to reduce the amount of  $\beta\text{Sn}$  impurities improving electrochemical performances, even at high C-rates.
- Study of electrochemical reactions by *in situ*  $^{119}\text{Sn}$  Mössbauer spectroscopy and X-ray photoelectron spectroscopy.
- First discharge: restructuring step that transforms the pristine material into  $\text{Mn/Li}_7\text{Sn}_2$  nanocomposite.
- Charge: de-alloying of  $\text{Li}_7\text{Sn}_2$  followed by the back reaction of Mn with poorly lithiated  $\text{Li}_x\text{Sn}$  alloys.

## ARTICLE INFO

### Article history:

Received 27 October 2012

Received in revised form

10 January 2013

Accepted 17 January 2013

Available online 28 January 2013

### Keywords:

$\text{MnSn}_2$

Intermetallic

Anode

Li-ion

Mössbauer spectroscopy

XPS

## ABSTRACT

A synthesis method consisting of a mechanical ball milling activation process followed by a sintering heating treatment is proposed to obtain  $\text{MnSn}_2$  as anode material for Li-ion batteries. This two-step approach strongly reduces the amount of  $\beta\text{Sn}$  impurities and provides a better material morphology. This improves the electrochemical performances, even at high C-rate, as shown from the comparison between electrode materials obtained with and without this preliminary activation process. The electrochemical reactions have been followed at the atomic scale by *in situ*  $^{119}\text{Sn}$  Mössbauer spectroscopy. The first discharge is a restructuring step that transforms the pristine material into  $\text{Mn/Li}_7\text{Sn}_2$  nanocomposite which should be considered as the real starting material for cycling. The delithiation of this nanocomposite is characterized by two plateaus of potential attributed to the de-alloying of  $\text{Li}_7\text{Sn}_2$  followed by the back reaction of Mn with poorly lithiated  $\text{Li}_x\text{Sn}$  alloys, respectively. The composition and the stability of the solid electrolyte interphase were characterized by X-ray photoelectron spectroscopy.

© 2013 Elsevier B.V. All rights reserved.

## 1. Introduction

Li-ion batteries are one of the most interesting electrochemical storage systems for applications in portable electronic devices or electrical vehicles because of their high power and energy densities compared to other rechargeable battery systems [1–3]. In order to increase the energy density, an extensive research is currently devoted to improve existing electrode materials such as carbon based materials for anodes. In addition, a lot of effort has been made to find new anode materials that can store more lithium than graphite. For example,  $\beta\text{Sn}$  materials have theoretical maximum specific and

volumetric capacities of  $994 \text{ mAh g}^{-1}$  and  $7200 \text{ mAh cm}^{-3}$ , respectively. In addition, tin is environmentally friendly, has a high packing density and an average alloying potential (vs.  $\text{Li}^+/\text{Li}^0$ ) higher than that of graphite, giving a battery with improved safety. However, such high capacities are obtained with alloying/de-alloying reactions between Li and Sn, which produces large volume variations of the active material that end with electrode material pulverization and exfoliation, and hence leads to poor cyclability [4].

The use of  $\text{MSn}_x$  intermetallic compounds, where M is a transition metal, has been proposed in order to overcome the electrode deterioration during cycling. The role of the metal, M, which is electrochemically inactive, is to buffer the volume variations and maintain electrical contacts between the particles of the composite electrode during the Li–Sn alloying and de-alloying reactions. Such mechanism is expected to improve cycling and electrode stability.

\* Corresponding author. Tel.: +33 4 67 14 45 48; fax: +33 4 67 14 33 41.

E-mail address: [lippens@univ-montp2.fr](mailto:lippens@univ-montp2.fr) (P.-E. Lippens).

Various tin intermetallic compounds such as  $\text{FeSn}_2$  [5–8],  $\text{Ni}_3\text{Sn}_4$ ,  $\text{CoSn}_2$  [9–12],  $\text{Cu}_6\text{Sn}_5$  [13] or  $\text{CrSn}_2$  [14] have been proposed as possible new anode materials for Li-ion batteries. Among the different transition metals, cobalt is certainly the most interesting and widely studied. It has been used, for example, with Sn and C to form nanostructured alloys as previously commercialized by Sony [15]. However, the substitution of Co, even partially, by another transition metal could be of interest to reduce the cost of the electrode material [16,17]. Iron has been proposed as a possible candidate and both the electrochemical mechanisms and performances of anodes containing microparticles or nanostructured materials have been extensively studied [5–8].

There are fewer studies about manganese which is another interesting metal to replace cobalt [18–20]. The electrochemical performances of Mn–Sn compounds are rather poor and better results have been obtained with Mn–Sn–C based electrodes [20]. In addition, the existence of tin atoms at grain boundaries of Mn–Sn inactive phases has been found to play a positive role in the cycling behavior of the electrodes. It is often difficult to obtain pure crystalline  $\text{MnSn}_2$  from synthesis methods including sintering heat treatment and metallic tin is generally found in addition to this compound [21]. In this work, we investigate a new synthesis method, including an initial mechanical ball milling activation followed by a sintering process, to obtain  $\text{MnSn}_2$  particles without  $\beta\text{Sn}$  impurities. Characterization and electrochemical performances of  $\text{MnSn}_2$  obtained without and with this activation step are given in this paper. A detailed analysis of the electrochemical mechanisms and of interfacial reactions based on *in situ*  $^{119}\text{Sn}$  Mössbauer spectroscopy and X-ray photoelectron spectroscopy (XPS), respectively, is also presented and the results are briefly compared to other tin based intermetallic compounds.

## 2. Experimental

$\text{MnSn}_2$  was prepared directly from micrometric Sn (Sigma–Aldrich, 99.5% purity) and Mn (Sigma–Aldrich, 99.5% purity). The stoichiometric amounts of manganese and tin powders (1.5 g) were charged in a 50 mL stainless steel grinding jar within an argon-filled glove box. The powder was mechanically milled (with a planetary ball mill) with 4 stainless steel balls of 5 g each during various periods. The ball milling was processed at 100, 200 and 400 rpm, respectively. To avoid high temperature produced during long time milling, the process was paused for 10 min every 15 min. The obtained powder was then wrapped under argon atmosphere, sealed in a quartz tube under dynamic vacuum, heated at 500 °C for 15 days and cooled down rapidly by water quenching to result in a final black product.

X-ray diffraction (XRD) was carried out to identify the obtained phases over the  $2\theta$  range from 10° to 90° by using a PHILIPS X'Pert MPD equipped with the X'celerator detector with Cu  $K_\alpha$  radiation ( $\lambda = 1.5418 \text{ \AA}$ ). The unit cell parameters were obtained from the diffraction patterns using the FULLPROF program [22]. The particle microstructure of the synthesized  $\text{MnSn}_2$  powders was observed by scanning electron microscope (SEM).

The electrodes used for the electrochemical tests were prepared by mixing 80 wt % active material with 10 wt % carbon black as electronic conductor and 10 wt % polyvinylidene fluoride (PVdF) as binder dissolved in *n*-methyl pyrrolidinone NMP and spread on a Cu foil substrate. The electrodes were pressed and dried for 12 h at 120 °C under vacuum to remove solvent and water. The electrodes were cut into disks with 7 mm in diameter and about 0.2 mm in thickness corresponding to an active mass of approximately 2 mg. Swagelok™ type cells were assembled in an argon-filled glove box using a glass microfiber paper separator (Whatman), 1 M  $\text{LiPF}_6$  dissolved in ethylene carbonate (EC) and dimethyl carbonate

(DMC), EC:DMC 1:1, as an electrolyte, and Li foil as a counter and reference electrode. All cells were tested within a fixed voltage window, between 0.01 and 1.2 V vs.  $\text{Li}^+/\text{Li}^0$ , under galvanostatic conditions at different C-rate regimes: C/10–10 C (1 C corresponds to the current of 1 Li/Sn in 1 h).

The electrodes used for XPS and Mössbauer spectroscopy were prepared by mixing 90 wt % active material with 10 wt % carbon black, without PVdF binder, for a better identification of surface carbonaceous species and to improve the *in situ* measurements, respectively. XPS measurements were carried out with a Kratos Axis Ultra spectrometer using a focused monochromatized Al  $K_\alpha$  radiation ( $h\nu = 1486.6 \text{ eV}$ ). For the Ag  $3d_{5/2}$  line, the full width at half maximum was 0.58 eV under the recording conditions. The binding energy scale was calibrated from the carbon contamination using the C 1s peak at 285.0 eV. Core peaks were analyzed using a nonlinear Shirley-type background. The peak positions and areas were optimized by a weighted least-square fitting method using 70% Gaussian, 30% Lorentzian lineshapes.

The  $^{119}\text{Sn}$  Mössbauer spectra were recorded in transmission geometry and constant accelerator mode at room temperature with a 5 mCi Ca  $^{119}\text{m}\text{SnO}_3$  source. The velocity scale was calibrated using the magnetic six-line spectrum of a high-purity iron foil absorber as a standard and using  $^{57}\text{Co(Rh)}$  as the source. The hyperfine parameters were determined with a non-linear least-square method, by using the program GM5SIT [23] and the Lorentzian profiles. The isomer shift values are given with respect to  $\text{BaSnO}_3$ .

## 3. Result and discussion

Preparation of  $\text{MnSn}_2$  by direct heating of metallic powders has been reported to give  $\beta\text{Sn}$  impurities in addition to  $\text{MnSn}_2$  [21]. In recent years, mechanical activation has been included in the synthesis process of different types of alloys due to its simplicity, low cost and facility to produce a great amount of materials. The mechanical preliminary activation process accelerates the reaction rate, induces mechanochemical transformations and mechanical alloying. It decreases the particle size of the pristine materials, increases the contact area and initiates the alloying reactions depending on the ball mill parameters. In order to improve the purity of the  $\text{MnSn}_2$  based anode material, we used such an approach by considering a two-step method based on mechanical ball milling of Sn and Mn powders followed by a sintering heat treatment at 500 °C for 2 weeks. The effect of the activation step was studied by varying both the ball milling duration (<3 days) and speed (100–400 rpm). For simplicity, only the material obtained with the activation process during 2 days at 400 rpm (sample B) is compared to the material obtained without this activation step (sample A). The powders were both heated at 500 °C, but during 8 and 2 weeks for samples A and B, respectively. The comparison between XRD patterns clearly shows the existence of  $\beta\text{Sn}$  in sample A but not in sample B (Fig. 1). The  $\beta\text{Sn}$  diffraction peaks became intense when the mechanical ball milling duration or speed is lowered. The other peaks of the XRD patterns can be assigned to  $\text{MnSn}_2$  and were indexed in a primitive tetragonal type-structure ( $I4/mcm$  space group) with  $a = 6.63 \text{ \AA}$  and  $c = 5.42 \text{ \AA}$  in agreement with previously reported values [24]. Mn and Sn atoms are located at the 4a and 8h crystallographic sites, respectively. The structure is similar to that of  $\text{FeSn}_2$  [25]. The Sn atoms are bonded to 4 Mn first-nearest neighbors located in the same basal plane. For both samples A and B, the observed narrow and symmetric Bragg lines indicate a good crystallinity of the  $\text{MnSn}_2$  powder. Analysis of the XRD patterns just after the mechanical ball milling activation shows partial formation of  $\text{MnSn}_2$  during this process for duration and speed higher than 2 days and 400 rpm, respectively, and highly dispersed Mn and Sn particles. This confirms that high energy activation increases the contact area between the particles resulting

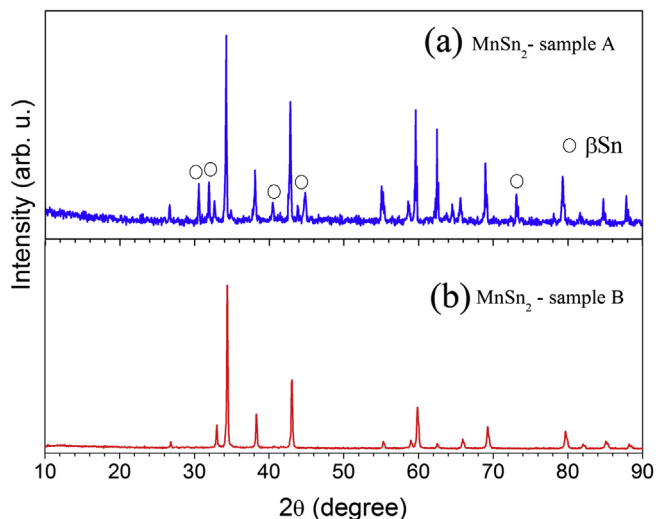


**Fig. 1.** X-ray diffraction patterns of sample A obtained without mechanical ball milling activation (a) and of sample B obtained with activation (b).

in high chemical activity. This promotes the formation of the alloys during heating and significantly reduces the amounts of unreacted Mn and  $\beta$ Sn in the final product. Longer milling times and higher speeds (up to 3 days/500 rpm) did not change noticeably the purity and the structural properties of the final product. This means that rather pure and well-crystallized  $\text{MnSn}_2$  samples can be obtained from elements after mechanical activation of about 2 days/400 rpm followed by a sintering heating treatment (sample B).

The SEM image of sample B shows that powder consists of agglomerated micrometric  $\text{MnSn}_2$  particles having a rather homogenous and porous morphology (Fig. 2a). At the opposite, the powder obtained with a shorter ball milling duration (1 day) and a lower speed (250 rpm) shows a more heterogeneous morphology with the presence of Mn (gray in Fig. 2b) and  $\beta$ Sn (white in Fig. 2b) impurities.

The room temperature  $^{119}\text{Sn}$  Mössbauer spectra of samples A (Fig. 3a) and B (Fig. 3b) are very different. The Mössbauer spectrum of sample A shows magnetic splitting due to Sn transferred hyperfine fields that can be fitted with two magnetic subspectra as previously described [21]. This is due to the antiferromagnetic behavior of bulk  $\text{MnSn}_2$  at room temperature. A third component is required to fit the experimental data that can be assigned to  $\beta$ Sn in agreement with XRD. The spectrum of sample B can be fitted with only one doublet which reflects the paramagnetic behavior of this

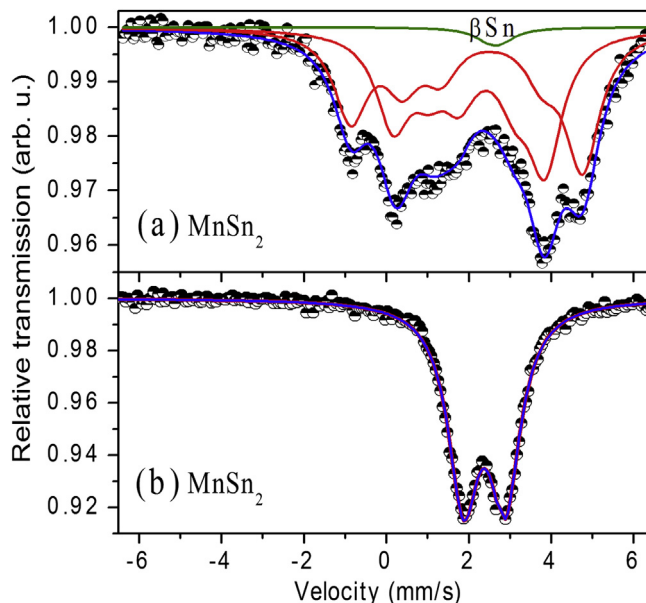


**Fig. 3.** Room temperature  $^{119}\text{Sn}$  Mössbauer spectra of  $\text{MnSn}_2$  sample A (a) and B (b).

sample. The linewidth ( $\Gamma = 0.9 \text{ mm s}^{-1}$ ) indicates that tin atoms occupy one crystallographic site in agreement with the crystal structure and the good crystallinity observed by XRD. For both samples, the values of isomer shift (IS) and quadrupole splitting (QS) are close and similar to published values [19,21]. The IS:  $\delta = 2.3 \text{ mm s}^{-1}$  is in the range of Sn(0) in intermetallic compounds and the rather large value of QS,  $\Delta = 1.08(1) \text{ mm s}^{-1}$ , is due to the strong asymmetric environment of the Sn atoms. Thus, the  $^{119}\text{Sn}$  Mössbauer spectroscopy confirms the existence of  $\beta$ Sn in sample A and reveals the absence of Sn transferred magnetic field in sample B. This could be due to some structural disorder caused by the mechanical activation, although such disorder should be small if we consider the XRD results or to the small size of the primary particles due to a better dispersion of the particles during mechanical ball milling and the heating time (2 weeks for sample B instead of 8 weeks for sample A).

The potential curves of the samples A and B were measured vs. metallic lithium anode at room temperature (Fig. 4). The two electrodes have been cycled between 0.1 and 1.2 V in galvanostatic mode at C/10 rate. The overall shapes of the two curves are similar and typical of tin based intermetallic compounds [7,11,12] with a low potential plateau for the first discharge ( $\sim 0.25 \text{ V}$ ) and

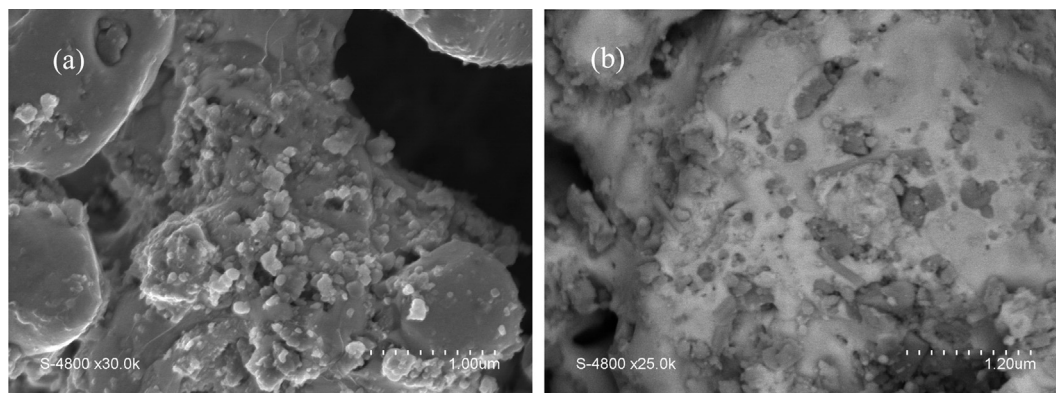


**Fig. 2.** SEM pictures of samples with ball milled activations at 400 rpm for 48 h (a) and 200 rpm for 24 h (b).

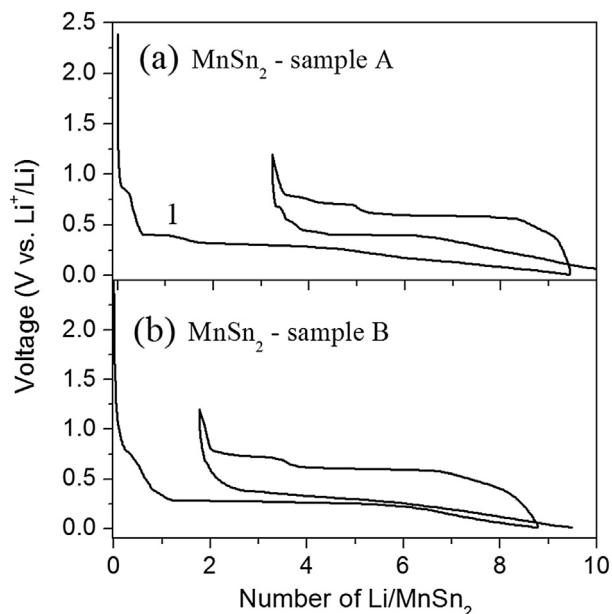


**Fig. 4.** First cycle voltage profiles of A (a) and B (b) based electrodes (80 wt % active material, 10 wt % carbon black and 10 wt % PVdF) in Swagelok cells with 1 M LiPF<sub>6</sub> dissolved in EC:DMC 1:1 electrolyte solution. Galvanostatic mode (at C/10: 1 Li per 10 h) and electrode potential range of 0.01–1.2 V vs. Li<sup>+</sup>/Li<sup>0</sup> were used in the two cases. The plateau labeled 1 in (a) is due to the transformation of βSn to Li<sub>x</sub>Sn alloys.

reversible cycles at higher average potential (~0.5 V). The polarization is of about 0.2 V. However, the sample A shows a progressive potential decrease during the first discharge (labeled 1 in Fig. 4a) that can be attributed to the progressive formation of Li<sub>x</sub>Sn alloys from βSn impurities. In addition, this sample exhibits a large irreversible capacity loss between the first discharge and the first charge that can be partially due to the existence of βSn and to the poor dispersion of the active material within the composite electrode, leading to loss of electrical contacts caused by volume variations during lithiation/delithiation reactions. Fig. 5 shows a comparison between the cycling performances (specific capacity

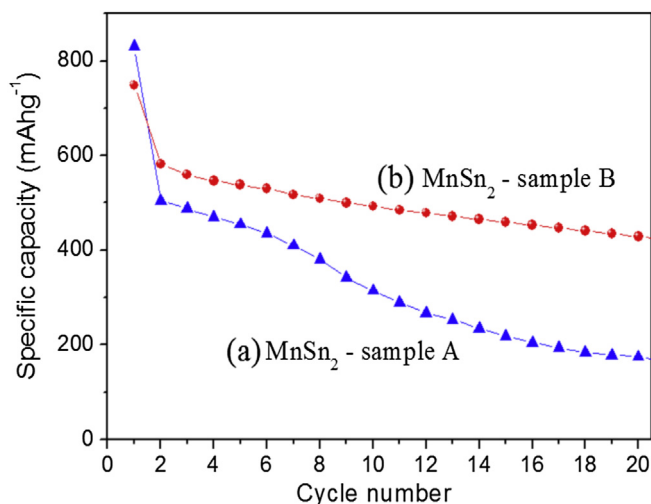
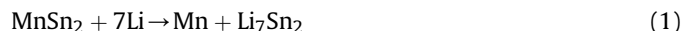


**Fig. 5.** Comparison between the specific capacities of samples A and B as a function of cycle number at C/2 (1 C = 1 Li per hour) in galvanostatic mode. Swagelok cells with A and B based electrodes (80 wt % active material, 10 wt % carbon black and 10 wt % PVdF) and 1 M LiPF<sub>6</sub> dissolved in EC:DMC 1:1 electrolyte solution were used. The electrode potential range was 0.01–1.2 V vs. Li<sup>+</sup>/Li<sup>0</sup>.

as a function of cycle number) of samples A and B at C/2. There is a strong decrease of the specific capacity from the first to the second cycle due to the irreversible capacity loss as observed in the potential curves (Fig. 4). Then, the capacity fade is more important for sample A than for sample B. The capacity of the former sample is of about 200 mAh g<sup>-1</sup> after 20 cycles, which is lower than that of carbon based anodes. Since the electrode preparation and the electrochemical tests were similar for the two samples, these poor performances are clearly due to the composition (existence of βSn impurities) and the morphology of the sample A. A similar behavior was also observed at higher current densities. Thus, the sample B, with rather pure MnSn<sub>2</sub> active material, shows better performances than A. This can be related to both the quality of the pristine material and the transformation of the electrode composite during the first discharge.

The first discharge is a crucial step in the cycling behavior of tin intermetallic composite electrodes and concerns here about 8 Li/MnSn<sub>2</sub>. The *in situ* <sup>119</sup>Sn Mössbauer spectra obtained during the first discharge for sample B show the progressive transformation, after about 1 Li/MnSn<sub>2</sub>, of the doublet of the paramagnetic MnSn<sub>2</sub> into a single peak that can be attributed to Li<sub>7</sub>Sn<sub>2</sub> (Fig. 6) as for FeSn<sub>2</sub> [7]. This indicates that the low potential plateau of the first discharge is due to the conversion reaction:



This is a direct transformation of MnSn<sub>2</sub> into the Li-rich Li<sub>7</sub>Sn<sub>2</sub>, without intermediate Li<sub>x</sub>Sn alloys as observed for βSn, with the extrusion of Mn transforming the pristine electrode into a Mn/Li<sub>7</sub>Sn<sub>2</sub> nanocomposite. In this composite, both the electrochemically active Li<sub>7</sub>Sn<sub>2</sub> and the inactive Mn nanoparticles are highly dispersed, which favors the buffering effect of volume variations during alloying/de-alloying reactions of Li with Sn. There is no change in the Mössbauer spectra at the beginning of the first discharge (<1 Li) but the potential curve shows a plateau at about 0.9 V (Fig. 4) that can be attributed to the formation of the solid electrolyte interphase (SEI) as confirmed by XPS. The survey spectrum of the pristine electrode shows that the amount of oxygen detected by XPS is of about 34% at. (Fig. 7). This is due to oxidation of the metals leading to the formation of tin and manganese oxides at the particle surface that are expected to react irreversibly with lithium during the first discharge. However, this concerns a small amount of atoms and the contribution to the irreversible mechanism is weak. The C 1s XPS spectra for x > 0.5 Li show a weak component at 283 eV, assigned to carbon black, whereas it is the

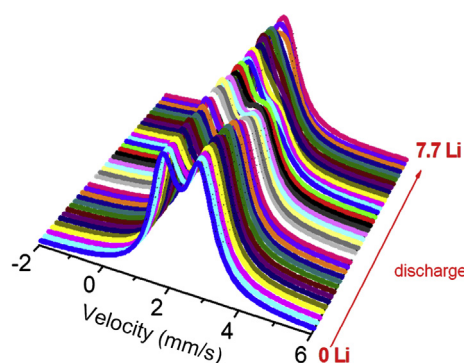


**Fig. 6.** *In situ* <sup>119</sup>Sn Mössbauer spectra (fitted curves) of MnSn<sub>2</sub> (sample B) during the first discharge in galvanostatic mode at C/10 (1 C = 1 Li per hour). Swagelok type cell with B based powdered electrode (90 wt % active material, 10 wt % carbon black) and 1 M LiPF<sub>6</sub> dissolved in EC:DMC 1:1 electrolyte solution were used. The electrode potential range was 0.01–1.2 V vs. Li<sup>+</sup>/Li<sup>0</sup>.



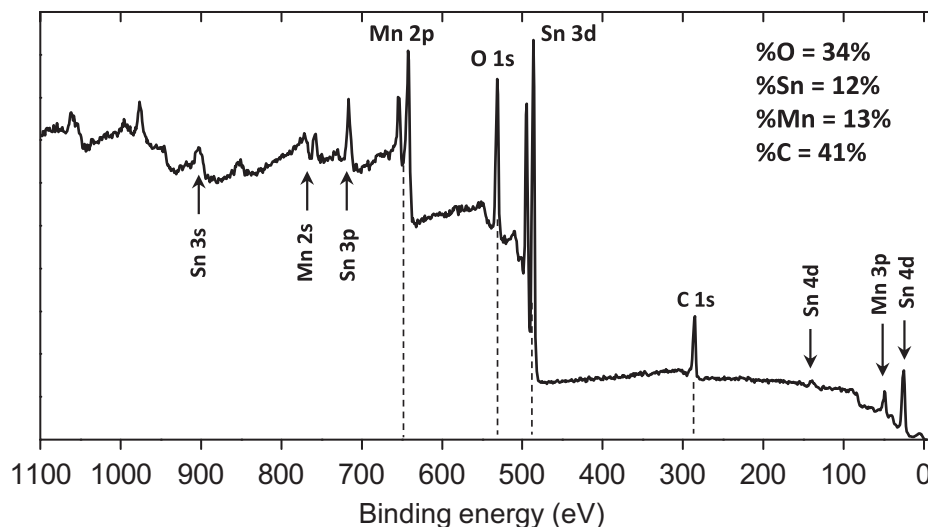


Fig. 7. XPS survey spectrum of pristine  $\text{MnSn}_2$  material, with corresponding atomic percentages of elements at the surface (Auger peaks are not depicted in the figure).

main component for the pristine electrode (Fig. 8). The other C 1s components at about 285, 286.5, 288.5 and 290 eV, observed at  $x = 0.5$  Li and during further discharge, correspond to carbon atoms in  $\text{CH}_2$ , C–O, O=C–O and  $\text{CO}_3$ -like environments, respectively.

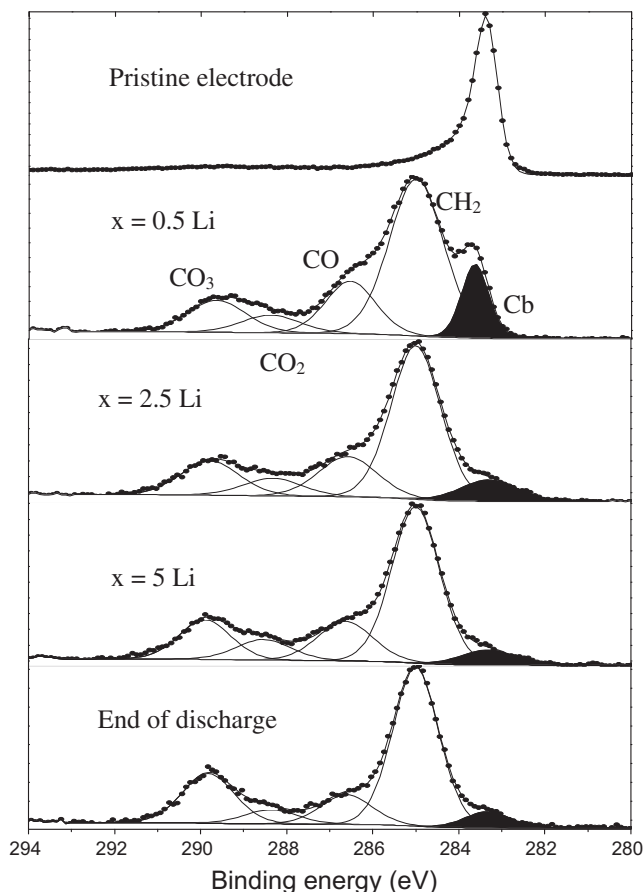
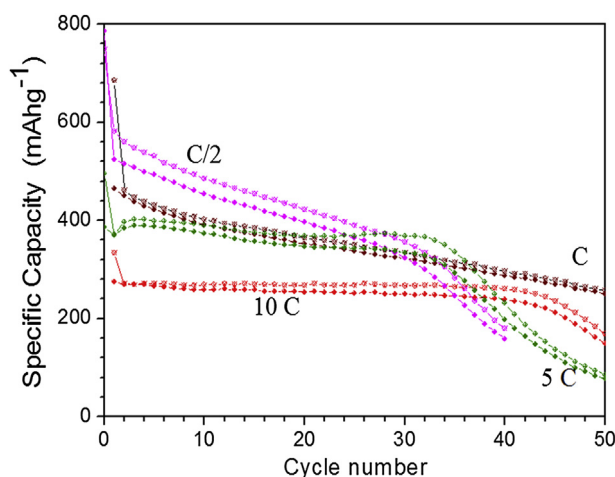


Fig. 8. C 1s XPS spectra of  $\text{MnSn}_2$  (sample B) at different stages of lithiation during the first discharge performed in galvanostatic mode at C/10 (1 C = 1 Li per hour). Swagelok cells with B based powdered electrode (90 wt % active material and 10 wt % carbon black) and 1 M  $\text{LiPF}_6$  dissolved in EC:DMC 1:1 electrolyte solution were used. The electrode potential range was 0.01–1.2 V vs.  $\text{Li}^+/\text{Li}^0$ .

They display the formation of carbonaceous species making up the SEI, resulting from the degradation of the electrolyte solvents at the surface of the electrode [26]. The intensity of the C1s peak of carbon black strongly decreases at the very beginning of the discharge ( $x < 0.5$  Li) due to the covering process of the electrode by the SEI film. Note that a decrease of the Sn  $3d_{5/2}$  peak intensity assigned to  $\text{MnSn}_2$  is also observed, indicating the formation of SEI at the  $\text{MnSn}_2$  particle surface as previously observed for other tin-based intermetallic compounds such as  $\text{Cu}_6\text{Sn}_5$  [13] or  $\text{Ni}_3\text{Sn}_4$  [26,27]. All the C 1s spectra observed during the first discharge have very close peak intensity ratios (except for carbon black). This indicates that the SEI and its composition are stable during the lithiation of the pristine electrode. Thus, the first discharge of sample B leads to the *in situ* formation of  $\text{Mn/Li}_7\text{Sn}_2$  nanocomposite electrode with a stable SEI obtained at the beginning of this process. At the end of the first discharge, this nanocomposite can be considered as the real starting electrode for cycling.

The charge process is more complex. The potential curve show two plateaus at about 0.6 V ( $4 \text{ Li} < x < 7 \text{ Li}$ ) and 0.7 V ( $2 \text{ Li} < x < 3.5 \text{ Li}$ ), respectively (Fig. 4b). Some first results obtained by *in situ* Mössbauer spectroscopy suggest that the first plateau is due to the delithiation of  $\text{Li}_7\text{Sn}_2$  and the second plateau to the back reaction of Mn with poorly lithiated  $\text{Li}_x\text{Sn}$  alloys. This mechanism differs from that of  $\text{FeSn}_2$  which is based on alloying reactions without back reaction of Fe (at lithium rate higher than C/10) but it looks like that of  $\text{CoSn}_2$  and  $\text{Ni}_3\text{Sn}_4$  which show back reaction of the transition metals with tin. In the latter case,  $\text{Ni}_3\text{Sn}_4$  is reformed at the end of charge while Li–Co–Sn alloys are formed during the charge of  $\text{CoSn}_2$  based electrodes [12]. The nanocomposite, transition metal/ $\text{Li}_7\text{Sn}_2$ , is reformed during the second discharge for all the transition metals. The next cycles are similar to the first charge–second discharge cycle. Thus, the delithiation mechanisms depend on the type of transition metal. This is probably related to the energy of the M–Sn chemical bonds which depends on M. The existence of a ternary phase is not clearly observed for  $\text{MnSn}_2$ , as in the case of  $\text{Mn}_2\text{Sb}$  [28] or  $\text{MnSb}$  [29], but further works are needed to investigate in detail the charge mechanism.

The variations of the specific capacity of  $\text{MnSn}_2$  based electrodes (sample B) as a function of the cycle number are plotted in Fig. 9 for different Li rates (C/2–10 C). There is a strong decrease in the capacity from the first to the second cycle due to the irreversible capacity loss between the first discharge and the first charge. The



**Fig. 9.** Specific capacity of  $\text{MnSn}_2$  (sample B) as a function of cycle number at different C rates (1 C = 1 Li per hour) in galvanostatic mode. Swagelok cells with B based electrodes (80 wt % active material, 10 wt % carbon black and 10 wt % PVdF) and 1 M  $\text{LiPF}_6$  dissolved in EC:DMC 1:1 electrolyte solution were used. The electrode potential range was 0.01–1.2 V vs.  $\text{Li}^+/\text{Li}^0$ .

average capacity over the first 30 cycles decreases from about  $500 \text{ mAh g}^{-1}$  (at C/2) to  $300 \text{ mAh g}^{-1}$  (at 10 C), which is consistent with kinetic effects of the conversion/alloying reactions at high Li rates. It is worth noting that capacity decreases continuously at low lithium rate (C/2, C) and is rather constant for higher rates (5 C, 10 C) but decreases abruptly at about 40 cycles as previously observed for  $\text{FeSn}_2$ , even with different binder or conductive materials [30]. This indicates a rapid loss of conductive contacts due to volume variations in the alloying/de-alloying processes for  $\text{Li}_x\text{Sn}$  [18] while this loss is more progressive at low Li rate. However, the capacity retention is better than that of  $\beta\text{-Sn}$  [7]. This confirms the buffering effect of Mn in the electrochemical processes as observed for  $\text{FeSn}_2$  [7] but there is also here a back reaction of Mn with Sn that tends to trap poorly lithiated tin particles and maintains dispersion within the composite electrode.

#### 4. Conclusion

$\text{MnSn}_2$  has been synthesized by a two-step method including mechanical ball milling activation process followed by a sintering heating treatment in order to reduce the amount of  $\beta\text{Sn}$  impurities. Improved electrochemical performances, even at high C-rates, have been observed for  $\text{MnSn}_2$  obtained with activation process due to the absence of impurities and to the morphology of the material. The analysis of the mechanisms shows that discharges correspond to the direct formation of a  $\text{Mn/Li}_7\text{Sn}_2$  nano-composite and the charges to the progressive delithiation of  $\text{Li}_7\text{Sn}_2$  and back reaction with Mn. Although improvement of the capacity

retention requires a better formulation of the composite electrode (binder, conductive additive) or of the electrolyte, as in the case of the other tin intermetallic compounds, this study indicates that Mn can substitute for Co but leads to more complex electrochemical mechanisms.

#### Acknowledgments

This work has been carried out in the framework of the European Research Institute ALISTORE. A. Mahmoud acknowledges the support from the Agence Universitaire de la Francophonie (AUF).

#### References

- [1] A.N. Jansen, A.J. Kahaian, K.D. Kepler, P.A. Nelson, K. Amine, D.W. Dees, D.R. Visser, M.M. Thackeray, *J. Power Sources* 81–82 (1999) 902.
- [2] A.F. Burke, *Proc. IEEE* 95 (2007) 806.
- [3] J.M. Tarascon, *Philos. Trans. R. Soc., A* 368 (2010) 3227.
- [4] J.O. Besenhard, J. Yang, M.J. Winter, *J. Power Sources* 68 (1997) 87.
- [5] O. Mao, R.L. Turner, I.A. Courtney, B.D. Fredericksen, M.I. Buckett, L.J. Krause, J.R. Dahn, *Electrochem. Solid State Lett.* 2 (1999) 3.
- [6] R.A. Dunlap, O. Mao, J.R. Dahn, *Phys. Rev. B* 59 (1999) 3494.
- [7] M. Chamas, P.E. Lippens, J.C. Jumas, K. Boukema, R. Dedryvère, D. Gonbeau, J. Hassoun, S. Panero, B. Scrosati, *J. Power Sources* 196 (2011) 7011.
- [8] M. Chamas, P.E. Lippens, J.C. Jumas, J. Hassoun, S. Panero, B. Scrosati, *Electrochim. Acta* 56 (2011) 6732.
- [9] P.P. Ferguson, M. Rajora, R.A. Dunlap, J.R. Dahn, *J. Electrochem. Soc.* 156 (2009) A204.
- [10] J. Li, D.B. Le, P.P. Ferguson, J.R. Dahn, *Electrochim. Acta* 53 (2010) 2991.
- [11] S. Naille, C.M. Ionica-Bousquet, F. Robert, F. Morato, P.E. Lippens, J. Olivier-Fourcade, *J. Power Sources* 174 (2007) 1091.
- [12] C.M. Bousquet, P.E. Lippens, L. Aldon, J. Olivier-Fourcade, J.C. Jumas, *Chem. Mater.* 18 (2006) 6442.
- [13] S. Naille, R. Dedryvère, S. Leroy, H. Martinez, P.E. Lippens, J.C. Jumas, D. Gonbeau, *J. Power Sources* 174 (2007) 1086.
- [14] M.Z. Xue, Z.W. Fu, *Solid State Ionics* 177 (2006) 1501.
- [15] Sony, U.S. Patent 0053131, 2005.
- [16] P.P. Ferguson, P. Liao, R.A. Dunlap, J.R. Dahn, *J. Electrochem. Soc.* 56 (2009) A13.
- [17] U.G. Nwokeke, A.V. Chadwick, R. Alcántara, M. Alfredsson, J.L. Tirado, *J. Alloys Compd.* 509 (2011) 3074.
- [18] L. Beaulieu, J.R. Dahn, *J. Electrochem. Soc.* 147 (2000) 3237.
- [19] L. Beaulieu, D. Larcher, R.A. Dunlap, J.R. Dahn, *J. Alloys Compd.* 297 (2000) 122.
- [20] P.P. Ferguson, L.L. Martine, A.E. George, J.R. Dahn, *J. Power Sources* 194 (2009) 794.
- [21] G. Le Caër, B. Malaman, G. Venturini, I.B. Kim, *Phys. Rev. B* 26 (1982) 5085.
- [22] J. Rodríguez-Carvajal, *Physica B* 192 (1993) 55.
- [23] K. Ruebenbauer, K.T. Birchall, *Hyperfine Interact.* 7 (1979) 175.
- [24] Y. Dong, F.J. DiSalvo, *Acta Crystallogr. E* 61 (2005) 282.
- [25] M. Armbrüster, M. Schmidt, R. Cardoso-Gil, H. Borrmann, Y.Z. Grin, *Kristallogr. NCS* 222 (2007) 83.
- [26] K.K.D. Ehinon, S. Naille, R. Dedryvère, P.E. Lippens, J.C. Jumas, D. Gonbeau, *Chem. Mater.* 20 (2008) 5388.
- [27] S. Naille, R. Dedryvère, D. Zitoun, P.E. Lippens, *J. Power Sources* 189 (2009) 806.
- [28] L. Häggström, C. Ionica, J.C. Jumas, L. Aldon, P.E. Lippens, K. Edström, *Hyperfine Interact.* 167 (2006) 759.
- [29] C. Ionica, M. Womes, P.E. Lippens, J. Olivier-Fourcade, B. Ducourant, A. Chadwick, *Hyperfine Interact.* 167 (2006) 773.
- [30] V. Sivasankaran, C. Marino, M. Chamas, P. Soudan, D. Guyomard, J.C. Jumas, P.E. Lippens, L. Monconduit, B. Lestriez, *J. Mater. Chem.* 21 (2011) 5076.